Parametric and V&V study in a fundamental CFD process: revisiting the lid-driven cavity flow

Mingming Ge

Kevin T. Crofton Department of Aerospace and Ocean Engineering, Virginia Polytechnic Institute and State University, Blacksburg, Virginia, USA

Xin-Lei Zhang

The State Key Laboratory of Nonlinear Mechanics, Institute of Mechanics, Chinese Academy of Sciences, Beijing, China, and

Kaleb Brookshire and Olivier Coutier-Delgosha

Kevin T. Crofton Department of Aerospace and Ocean Engineering, Virginia Polytechnic Institute and State University, Blacksburg, Virginia, USA

Abstract

Purpose – The openings on aircraft structures can be modeled from an aerodynamical point of view as lid-driven cavities (LDC). This paper aims to show the primary verification and validation (V&V) process in computational fluid dynamics (CFD, and to investigate the influences of numerical settings on the efficiency and accuracy for solving the LDC problem.

Design/methodology/approach – To dig into the details of CFD approaches, this paper outlines the design, implementation, V&V and results of an efficient explicit algorithm. The parametric study is performed thoroughly focusing on various iteration methods, grid density discretization terms and Reynolds number effects.

Findings – This study parameterized the numerical implementation which provides empirical insights into how computational accuracy and efficiency are affected by changing numerical settings. At a low Reynolds number (not over 1,000), the time-derivative preconditioning is necessary, and k = 0.1 can be the optimal value to guarantee the efficiency, as well as the stability. A larger artificial viscosity (c = 1/16) would relieve the calculating oscillation issue but proportionally increase the discretization error. Furthermore, the iteration method and the mesh quality are two key factors that affect the convergence efficiency, thus need to be selected "wisely".

Practical implications – The study shows how numerical implementation can enhance an accurate and efficient solution. This workflow can be used to determine the best parameter settings whenever CFD researchers applying this LDC problem as a complementary design tool for testing newly developed solvers.

Originality/value – The studied LDC problem is representative of CFD analysis in real aircraft structures. These numerical simulations provide a cost-effective and convenient tool to understand the parameter sensitivity, solution receptivity and physics of the CFD process.

Keywords Lid-driven cavity, Fluid dynamics, Computational fluid dynamics, Numerical method, Verification and validation

Paper type Research paper

Nomenclature

Symbols

B = time-derivative preconditioning parameter;
$C^{(4)}$ = fourth derivative constant in artificial viscosity;
Δt_c = convective stability time limit;
Δt_d = diffusive stability time limit;
f = source term of manufactured solution;
κ = prescribed number to limit β;
λ = eigenvalue term in artificial viscosity;
p = pressure, Pa;
ρ = density, kg/m³;
S = artificial viscosity;
u = x-component of velocity, m/s;
U_{lid} = driven velocity of the lid, m/s; and
v = y-component of velocity, m/s.

Definitions, Acronyms and Abbreviations

AR = aspect ratio;
CFD = computational fluid dynamics;
CFL = Courant– Friedrichs–Lewy;
DE = discretization error;
DSE = downstream secondary eddy;
FD = finite difference;
FE = finite element;

FV   = finite volume;
LDC   = Lid-driven cavity;
MMS   = method of manufactured solution;
NSE   = Navier-Stokes equation;
OOA   = observed order of accuracy;
PJ   = point Jacobi method;
Re   = Reynolds number;
SIMPLE = semi-implicit method for pressure-linked
             equations;
SGS   = symmetric Gauss-Seidel method; and
USE   = upstream secondary eddy.

1. Introduction

The lid-driven cavity (LDC) flow is not only technically important but also of great scientific interest because it displays almost all fluid mechanical phenomena in the simplest of geometrical settings (Perumal and Dass, 2011). In the fields of aerospace, LDC appears as the open surface of an airplane (for example, weapon bay doors of a jet fighter), which has the potential generating strong acoustic waves and resonance that decrease flight efficiency or can damage components. Another classical LDC issue is the aerodynamical noise generation due to the cavity of landing gear during take-off and landing. Therefore, experimental and numerical studies are essential to understand and control this fundamental flow in relevant to aerodynamics applications and academic research (Abderrahmane et al., 2019).

As sketched in Figure 1, the LDC flow is the motion of a fluid inside a rectangular cavity created by a constant translational velocity of one side while the other sides remain at rest. A rectangular container is among the most elementary confined geometries of fluid motion. And the simplest mechanical driving force acting on a fluid is the tangential in-plane motion of a bounded wall (Kuhlmann and Romanò, 2019). This geometrical simplicity facilitates abundant experimental

Figure 1 LDC flow

calibrations and benchmark data for comparison and validation (Gaikwad et al., 2021).

With the advancement of computational fluid dynamics (CFD) in the aerospace industry (Groth et al., 2019), CFD methods have been used with the most popularity to study the cavity flow, as some pioneer works of Burggraf (1966). Afterward, the most famous benchmark results are presented by Ghia et al. (1982), which has served as "The" result to compare against ever since. They solved the steady two-dimensional flow in a square cavity with boundary conditions of three rigid walls and a lid moving with constant velocity. These benchmark data are computed using a second-order accurate scheme, with a Reynolds number up to 10^4 in the mesh level of 257×257.

From the 1990s (Chiang et al., 1998), two-dimensional numerical analyses reveal the large-scale flow characteristics prevailing in the cavity, such as primary and secondary eddies, Reynolds number of transitions. Because realistic flows are three-dimensional, it is still necessary to apply three-dimensional numerical simulation to investigate physical subtleties in LDC. Since the 2000s, the use of a three-dimensional (3D) model for CFD simulation has been growing steadily because of technological advances in computer tools. Albensoeder and Kuhlmann (2005) extended the method of Botella and Peyret (1998) to three dimensions and investigated cases for different cavity lengths in the spanwise direction. They also applied different rigid and periodic boundary conditions at the end walls, and provided highly accurate 3D flow fields for Re = 10^3. At a high Reynolds number of 12,000, when the transition happens and turbulent model shall be applied, Bouffanais et al. (2007) carried out the large-eddy simulations with spectral element methods to compute the turbulent flow in a 3D cubical LDC. Other types of cavities are also investigated numerically, such as Xia et al. (2019), who applied an O-H-type grid, to avoid experimental complexity.

For the development of discretization schemes, besides the Finite Difference method, other methods emerged chronologically as listed by AbdelMigid (2017), such as (FE) Finite Element (Goetzendorf-Grabowski and Mieloszyk, 2017), Finite Volume (FV) (Gaikwad et al., 2021), Modified Differential Quadrature, Lattice Boltzmann (Perumal and Dass, 2011), Incremental Unknowns, Discrete Singular Convolution, (Cheb.) Chebyshev collocation, Boundary Element, Smooth Particle Hydrodynamic and Control Volume Finite Element Method. Among the above, the FV and the FE methods take second and third place in the popularity of fluid or solid simulations (Zhang et al., 2021; Ge et al., 2020). And benchmark results for cavity flow can be found in works by Magalhães (2013) and Barragy and Carey (1997).

Experimental investigations on LDC flow are always undergoing a parallel development with CFD, from the 1980s until recently (Sahak et al., 2020). Although with a certain geometrical simplicity, the flow physics inside this LDC is not such simple. Several flow characteristics which prevail in processing industries, such as boundary layers, eddies of different sizes and characteristics, and various instabilities, may coexist (Chiang et al., 1998). Koseff (1983) experimentally observed that the regular or periodic unsteadiness for LDC flow is no longer sustained and evolves into turbulence when the Reynolds number reaching the 6,000–8,000 range. Their
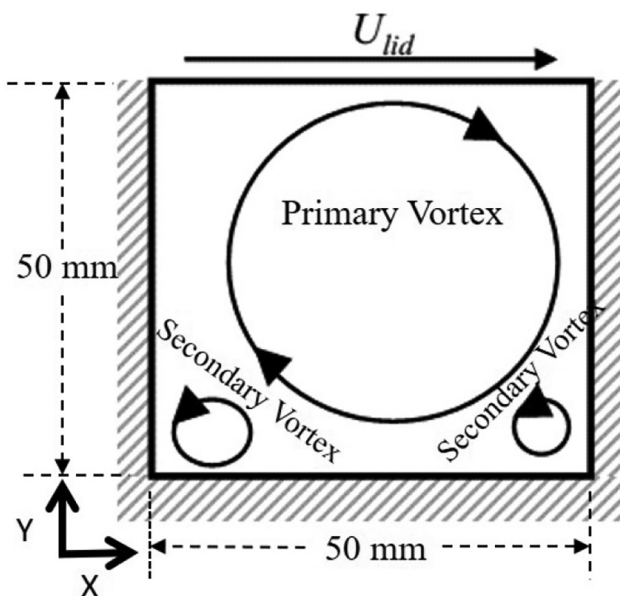
results provide a benchmark for the transitional Re and were confirmed by many numerical solutions obtained with Reynolds numbers up to 10^4 (Hammami *et al.*, 2018; Suman *et al.*, 2019).

In recent, the problem of rectangular LDC flow is investigated toward many new extensions such as considering mixed convection with heat transfer. Another prevailing area is the control of cavity acoustics actively or passively on a range of Mach numbers when the flow passing over a cavity such as the landing gear (Abderrahmane *et al.*, 2019). Other natural extensions concern the variation of the cavity shape or dimensions at the micro/nano scales where the Navier-stokes equation (NSE) loses its validity (Mmukherjee *et al.*, 2019). A pioneering parametric study showed the effects of different Reynolds numbers, lid velocity, cavity geometry and aspect ratio on the LDC flow behavior at the macro/micro-scale can be found in the literature (Shankar and Deshpande, 2000).

As succinctly stated by Shankar and Deshpande (2000) and quoted by Abdelmigid (2017), the importance of cavity flow case lies in that as follows:

> "[...] internal recirculating flows generated by the motion of one or more of the containing walls [...] are not only technologically important, but they are also of great scientific interest because they display almost all fluid mechanical phenomena in the simplest of geometrical settings. Thus, corner eddies, longitudinal vortices, nonuniqueness, transition, and turbulence all occur naturally and can be studied in the same closed geometry".

In summary, it has been shown that the cavity flow simulation has been highly developed especially in the past several decades, typically with higher and higher Reynolds numbers such as Re = 21,000 by Erturk *et al.* (2005; Erturk, 2009) and grid density such as $2,049 \times 2,049$ by Suman *et al.* (2019). Needless to say, most commercial CFD software can derive the refined solution conveniently nowadays. During the authors' research experiences, nevertheless, some subtle parameters inside those numerical packages are still unclear for many graduate students or entry-level engineers. It is in this light that we have been stimulated to work on this numerical parametric study in a fundamental 2 D square LDC flow, taking advantage of its unambiguous boundary conditions and simple geometry.

Instead of developing newer methods for computing the NSE of LDC, as good results of its steady solutions are widely published and universally accepted, the aim is to shed some light on the details of parameter setting and help to understand the fundamentals behind numerical methods. Case studies of steady incompressible flow in LDC are investigated with a *Re* range from 100 to 1,000, without the need to consider the bifurcation issue. Results with a second-order spatially accurate are verified and validated from different sources. Effects of various parameters are detailed presented for the sake of serving as a benchmark data set for future works on the same problem.

The next section is devoted to describing the multigrid solver for the governing equations. An emphasis is given on the explanation of added discretization terms during the time and space discretization. The formulations of dimensions and properties are: driven velocity $U_{lid} = 1\ m/s$, wall lengths $L_x = L_y = 0.05\ m$ with the aspect ratio AR = 1, density $\rho = 1\ kg/m^3$, Reynolds numbers $Re = 100, 500, 1,000$. Using the concept of the Kolmogorov length scale, the baseline mesh resolution requirement can be estimated by $\frac{l}{\eta} = Re^{\frac{3}{4}}$, and generates 32×32, 106×106, 178×178 grid cases, accordingly.

2. Theory and implementation

This incompressible flow is governed by a set of three, nonlinear differential equations that are discretized and solved using time-marching algorithms. The approaches taken here include only explicit methods. The flowchart of this research is shown in Figure 2 which can be seen mostly as an explicit pressure rescaled equation scheme preceded by a grid generation. The numbered steps represent the iteration scheme and each step is composed of both discretization and solution of the resulted linear algebraic equation system. A point Jacobi method (PJ) and symmetric Gauss-Seidel method (SGS) are implemented for the comparison of numerical behavior. Time-derivative preconditioning is used to stabilize the methods, with the assumption that these terms will tend toward zero as the solution converges to a steady-state. Artificial viscosity is included to mitigate any even-odd decoupling that the solution may be prone to. Several methods are used to verify the accuracy of the methods and various solution sensitivities and accuracy studies are performed. Discretization and interpolation techniques will be explained in detail next.

2.1 Governing equations

The set of equations (1)–(3) describe a two-dimensional flow which is assumed to be incompressible, laminar and Newtonian. A brief description is summarized below and details for the CFD initialization can be found in the literature by Brindhadevi (2021). Equation (1) requires that mass be conserved through the flow and is often called the continuity equation. Equations (2) and (3) require that momentum be conserved in the flow and represent Newton's Second Law of motion. Together, these equations can be solved for pressure p; the x-component of velocity u; and the y-component of velocity v throughout the flow field. The fluid density ρ and the dynamic viscosity μ are constants here.

$$\frac{\partial \rho}{\partial t} + \rho \frac{\partial u}{\partial x} + \rho \frac{\partial v}{\partial y} = 0 \tag{1}$$

$$\frac{\partial(\rho u)}{\partial t} + \rho u \frac{\partial u}{\partial x} + \rho v \frac{\partial u}{\partial y} + \frac{\partial p}{\partial x} - \mu\left(\frac{\partial^2 u}{\partial x^2} + \frac{\partial^2 u}{\partial y^2}\right) = 0 \tag{2}$$

$$\frac{\partial(\rho v)}{\partial t} + \rho u \frac{\partial v}{\partial x} + \rho v \frac{\partial v}{\partial y} + \frac{\partial p}{\partial y} - \mu\left(\frac{\partial^2 v}{\partial x^2} + \frac{\partial^2 v}{\partial y^2}\right) = 0 \tag{3}$$

2.2 Time-derivative preconditioning

To solve the steady-state equations, a standard way is to march the time-dependent terms to approach the steady-state. For equations not containing time-dependent terms, pseudo time-derivative preconditioning can be added which enables reaching the steady-state faster. Although the time-derivative preconditioning destroys the time accuracy in the transient solutions, only the steady-state is of interest here. And as the time-marching solutions converge to steady-state and do not

Figure 2 Flowchart for enumeration algorithms
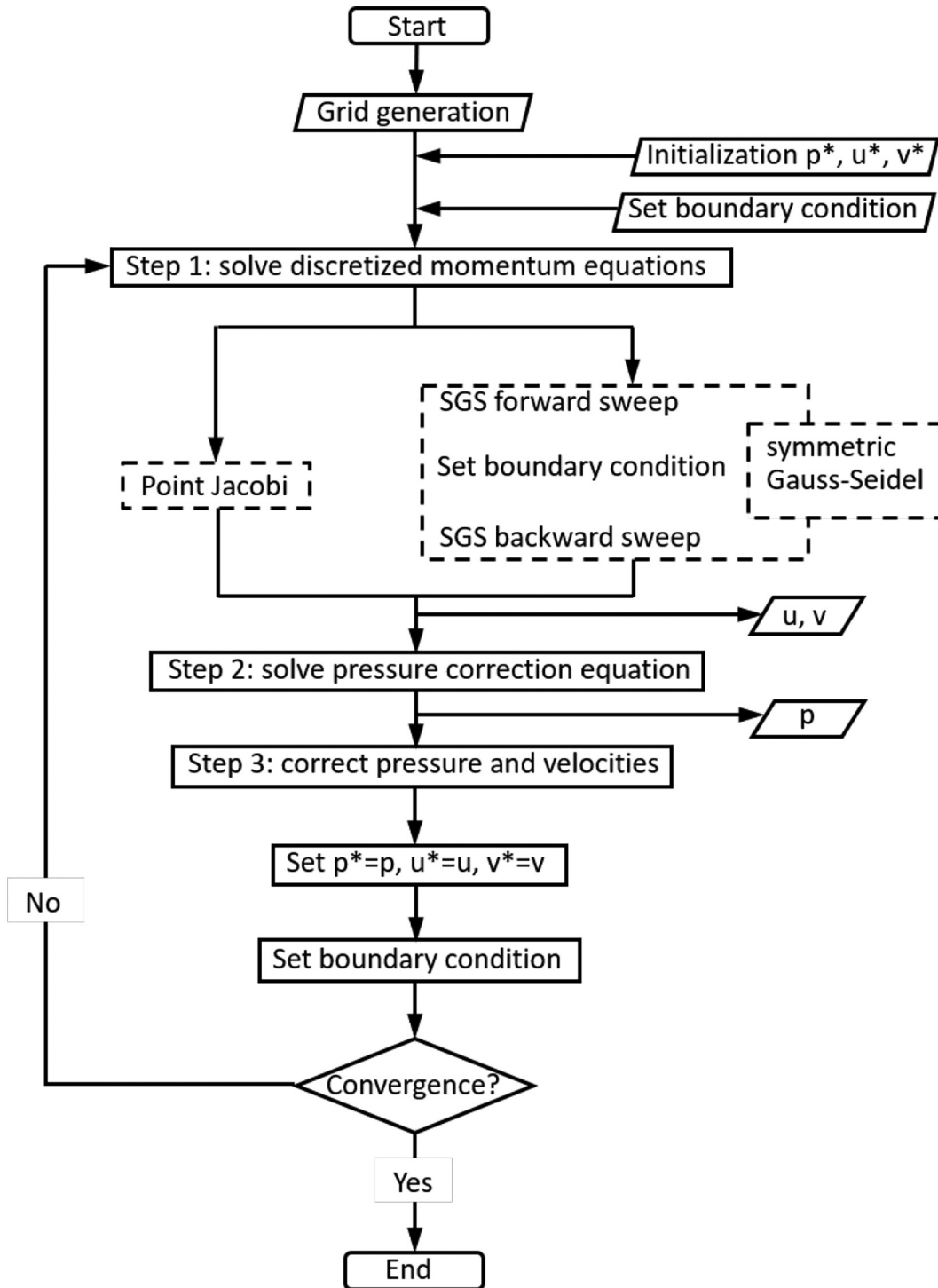
change significantly from one time step to the next, this pseudo time term will become negligibly small.

As the continuity equation for the incompressible flow does not contain any time derivatives, the pseudo-time derivative of the pressure term $\frac{1}{\beta^2}\frac{\partial p}{\partial t}$ is added to the left-hand side of the continuity equation (1). Without this preconditioning term, the system becomes ill-conditioned. The resulting modified equation is given in equation (4).

$$\frac{1}{\beta^2}\frac{\partial p}{\partial t} + \rho\frac{\partial u}{\partial x} + \rho\frac{\partial v}{\partial y} = 0 \tag{4}$$

The parameter by which this term is multiplied by, β^2, is called the AC parameter. AC term has no physical meaning but it is chosen to scale the eigenvalues of the system to the same order of magnitude so that an efficient convergence rate can be achieved. It must have units of velocity for the dimensional

consistency, for instance, $\beta^2 = \mu^2$. However, this formulation runs the risk of β^2 becoming too small and driving the system unstable. And Turkel and Vatsa (1994) showed that, in the interest of convergence rate, the AC parameter should be kept as close as possible to the local convective velocity. Therefore, we implement the formulation given in Equation (5) which limits β^2 from getting too small. Here, κ is a prescribed number which is typically less than one, indicated by Esfahanian and Akbarzadeh (2011). To further investigate the effect of the choice of this κ parameter, cases with different κ are studied and discussed in Section 4.3.

$$\beta^2 = \max\left(u^2 + v^2, \kappa U_{lid}^2\right) \tag{5}$$

2.3 Discretization

Although various higher-order discretization methods exist in the literature, from an intention of simplicity and sufficient accuracy, the most popular primitive variable formulation is applied here for the LDC flows. Therefore, a second-order central difference is used in space, and a first-order forward difference is used in time. The schemes can be seen in equations (6)–(8).
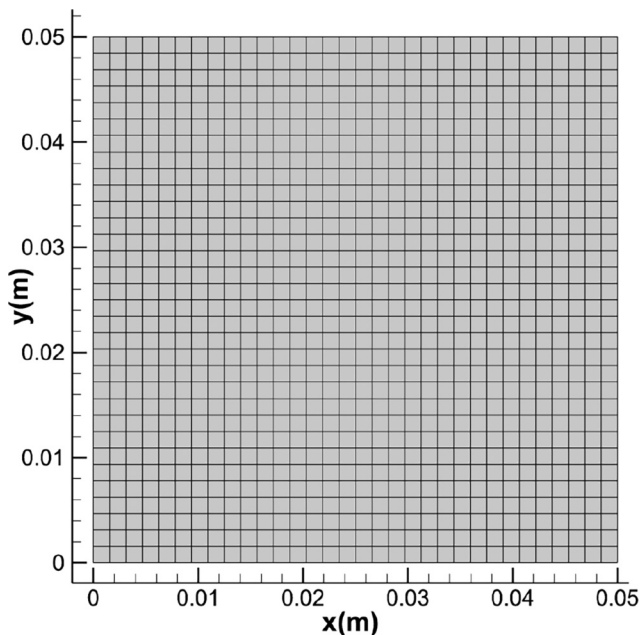
$$\frac{\partial p}{\partial t} = \frac{p_{i,j}^{n+1} - p_{i,j}^{n}}{\Delta t} \tag{6}$$

$$\frac{\partial u}{\partial x} = \frac{u_{i+1,j} - u_{i-1,j}}{2\Delta x} \tag{7}$$

$$\frac{\partial^2 u}{\partial y^2} = \frac{u_{i,j+1} - 2u_{i,j} + u_{i,j-1}}{(\Delta y)^2} \tag{8}$$

Here, the indices i and j refer to the nodes in a uniform and non-staggered mesh as can be seen in Figure 3. This represents

Figure 3 Example of a 33 × 33 numerical grid for discretizing the fluid domain

the discretized physical space for which the equations will be solved. The final discrete equations are represented in equations (9)–(10). Detailed discretization steps can be seen in the literature by Ghadge and Prakash (2021).

$$\frac{1}{\beta_{i,j}^2}\frac{p_{i,j}^{n+1} - p_{i,j}^{n}}{\Delta t} + \rho\left(\frac{u_{i+1,j}^{n} - u_{i-1,j}^{n}}{\Delta x} + \frac{v_{i+1,j}^{n} - v_{i-1,j}^{n}}{\Delta y}\right) = 0 \tag{9}$$

$$\frac{u_{i,j}^{n+1} - u_{i,j}^{n}}{\Delta t} + \rho\left(u_{i,j}\frac{u_{i+1,j} - u_{i-1,j}}{\Delta x} + v_{i,j}\frac{u_{i+1,j} - u_{i-1,j}}{\Delta y}\right) +$$
$$\frac{p_{i+1,j} - p_{i-1,j}}{2\Delta x} - \mu\left(\frac{u_{i+1,j} - 2u_{i,j} + u_{i-1,j}}{(\Delta x)^2} + \frac{u_{i,j+1} - 2u_{i,j} + u_{i,j-1}}{(\Delta y)^2}\right) = 0 \tag{10}$$

$$\frac{v_{i,j}^{n+1} - v_{i,j}^{n}}{\Delta t} + \rho\left(v_{i,j}\frac{v_{i+1,j} - v_{i-1,j}}{\Delta x} + u_{i,j}\frac{v_{i+1,j} - v_{i-1,j}}{\Delta y}\right) +$$
$$\frac{p_{i+1,j} - p_{i-1,j}}{2\Delta y} - \mu\left(\frac{v_{i+1,j} - 2v_{i,j} + v_{i-1,j}}{(\Delta x)^2} + \frac{v_{i,j+1} - 2v_{i,j} + v_{i,j-1}}{(\Delta y)^2}\right) = 0 \tag{11}$$

2.4 Stability criteria

The stability for this explicit method comes from a combination of the convective stability time limit and the diffusive time limit. The convective time step comes from the following equation (12):

$$\Delta t_c \leq \frac{\min(\Delta x, \Delta y)}{|\lambda|_{\max}} \tag{12}$$

where $|\lambda|_{\max} = \max(\lambda_x, \lambda_y)$, and $\lambda_x = \frac{1}{2}\left(|u_x| + \sqrt{u^2 + 4\beta^2}\right)$, $\lambda_y = \frac{1}{2}\left(|v_y| + \sqrt{v^2 + 4\beta^2}\right)$.

The diffusive time step is calculated from equation (13):

$$\Delta t_d \leq \frac{\Delta x \Delta y}{4v}, \qquad v = \mu/\rho \tag{13}$$

Then the stability time step limit can be obtained by combining the convective time step and the diffusive time step from equation (14):

$$\Delta t \leq \min(\Delta t_c, \Delta t_d) = CFL \cdot \min(\Delta t_c, \Delta t_d) \tag{14}$$

For the explicit methods, the Courant– Friedrichs–Lewy (CFL) number can be adjusted between zero and one based on the calculation convergence condition. In this study, the CFL is selected as 0.5 which generates a stable solution and was validated by Bruneau and Saad (2006).

2.5 Artificial viscosity

Notice that the continuity equation (9) does not have any kind of damping or diffusion term. With central differencing, the value at one node is based on the values at adjacent nodes but not necessarily on that node itself ("checkboard effect"). That is to say, the value at this node is slightly decoupled from its adjacent nodes and only even nodes are coupled with other

even ones, and vice versa for odd nodes. The local values can oscillate between nodes in a phenomenon often called odd-even decoupling. This issue can be mitigated by introducing an artificial viscosity term, S into the continuity equation as shown in equation (15).

$$\frac{1}{\beta_{i,j}^2}\frac{p_{i,j}^n - p_{i,j}^{n-1}}{\Delta t} + \rho\left(\frac{u_{i+1,j} - u_{i-1,j}}{\Delta x} + \frac{v_{i+1,j} - v_{i-1,j}}{\Delta y}\right) - S = 0 \tag{15}$$

Here, the artificial viscosity term S is proportional to the fourth derivative of pressure which must also be discretized by multiplying a constant $C^{(4)}$. Because the fourth derivative of pressure is small throughout the fluid flow, this term should be negligible upon convergence. The purpose of S is to re-couple the odd and even nodes. And the value of S is given through the equations (16) – (18), where $|\lambda_x|_{\max}$ is the magnitude of the largest eigenvalues in (x, t) space, $|\lambda_y|_{\max}$ is the magnitude of the largest eigenvalues in (y, t) space and typically $C^{(4)}$ ranges from $\frac{1}{128}$ to $\frac{1}{16}$.

$$S_{i,j} = S_{x(i,j)} + S_{y(i,j)}$$
$$= \frac{|\lambda_x|_{\max}C^{(4)}\Delta x^3}{\beta^2}\frac{\partial^4 p}{\partial x^4} + \frac{|\lambda_y|_{\max}C^{(4)}\Delta y^3}{\beta^2}\frac{\partial^4 p}{\partial y^4} \tag{16}$$

$$S_{x(i,j)} = \frac{\frac{1}{2}\left(|u_{i,j}| + \sqrt{u_{i,j}^2 + 4\beta^2}\right)C^{(4)}}{\beta^2\Delta x}$$
$$(p_{i+2,j} - 4p_{i+1,j} + 6p_{i,j} - 4p_{i-1,j} + p_{i+2,j}) \tag{17}$$

$$S_{y(i,j)} = \frac{\frac{1}{2}\left(|v_{i,j}| + \sqrt{v_{i,j}^2 + 4\beta^2}\right)C^{(4)}}{\beta^2\Delta y}$$
$$(p_{i,j+2} - 4p_{i,j+1} + 6p_{i,j} - 4p_{i,j-1} + p_{i,j+2}) \tag{18}$$

The values at the boundary condition which cannot be calculated with the fourth derivative will be duplicated directly from a nearby row or column. The values at four corners will be calculated as the average of nearby values.

2.6 Boundary conditions

To solve the equations within the computational domain, the boundary conditions are imposed at the edge nodes for each of the three variables p, u and v. The implement of velocity value is straightforward at boundary nodes as each component is set to zero for the left, right and bottom walls to impose a "no-slip" condition. The upper wall is set to have unity velocity in x and no y-component of velocity. Velocity components are then solved only on the inner nodes. Pressure boundary conditions are a bit more complicated as the value of pressure along the walls is nonzero and unknown. The condition that we impose here is that the second-order derivative of pressure normal to the wall is zero or the pressure gradient normal to the wall is constant. The pressure is solved for at the interior nodes and values at the boundary and then extrapolated via equation (19) for the bottom wall and equation (20) for the right wall, and similarly for the other boundaries. For each point at four corners, the boundary value is the average of nearby two points.

$$p_{i,1}^n = 2p_{i,2}^n - p_{i,3}^n \tag{19}$$

$$p_{\text{imax},j}^n = 2p_{\text{imax}-1,j}^n - p_{\text{imax}-2,j}^n \tag{20}$$

2.7 Time-marching algorithms

Two iteration methods are implemented for comparison purposes in this study. The first is a point Jacobi iterative method, which uses equations (21)–(23) with spatial derivative terms being evaluated at $n - 1$ to solve for p, u and v at a time step n. The Jacobi method is a so-called point-wise iteration method because the solution is updated sequentially node by node or point by point. As the right-hand side of the update formula uses only previous iteration values, the pattern used to sweep through the nodes in the computational domain is not relevant.

The other method used is the point SGS method, which updates the values in the special derivatives to be at the current time step n where possible. As this algorithm sweeps forward in the x-direction, only the values at $i - 1$ are updated and used, which can cause preference toward a certain side of the mesh. This issue can be solved by alternating the direction of sweeps during one iteration, that the SGS method first sweeps forward and then backward to produce a more "symmetric" algorithm. The convergence behavior of these two PJ and SGS methods will be discussed in the next Section 3.1.

$$p_{i,j}^{n+1} = p_{i,j}^n$$
$$-\beta_{i,j}^2\Delta t\left[\rho\frac{u_{i+1,j}^n - u_{i-1,j}^n}{2\Delta x} + \rho\frac{v_{i,j+1}^n - v_{i,j-1}^n}{2\Delta y} - S_{i,j} - f_{\text{mass}}(x,y)\right] \tag{21}$$

$$u_{i,j}^{n+1} = u_{i,j}^n - \frac{\Delta t}{\rho}\left[\rho u_{i,j}^n\frac{u_{i+1,j}^n - u_{i-1,j}^n}{2\Delta x} + \rho v_{i,j}^n\frac{u_{i,j+1}^n - u_{i,j-1}^n}{2\Delta y}\right.$$
$$+ \frac{p_{i+1,j}^n - p_{i-1,j}^n}{2\Delta x} - \mu\frac{u_{i+1,j}^n - 2u_{i,j}^n + u_{i-1,j}^n}{\Delta x^2}$$
$$\left. - \mu\frac{u_{i,j+1}^n - 2u_{i,j}^n + u_{i,j-1}^n}{\Delta y^2} - f_{xmtn}(x,y)\right] \tag{22}$$

$$v_{i,j}^{n+1} = v_{i,j}^n - \frac{\Delta t}{\rho}\left[\rho u_{i,j}^n\frac{v_{i+1,j}^n - v_{i-1,j}^n}{2\Delta x} + \rho v_{i,j}^n\frac{v_{i,j+1}^n - v_{i,j-1}^n}{2\Delta y}\right.$$
$$+ \frac{p_{i,j+1}^n - p_{i,j-1}^n}{2\Delta y} - \mu\frac{v_{i+1,j}^n - 2v_{i,j}^n + v_{i-1,j}^n}{\Delta x^2}$$
$$\left. - \mu\frac{v_{i,j+1}^n - 2v_{i,j}^n + v_{i,j-1}^n}{\Delta y^2} - f_{ymtn}(x,y)\right] \tag{23}$$

3. Model verification and validation

Verification and validation (V&V) are the primary means to assess accuracy and reliability in computational simulations. By Sargent (2013), model verification is defined as "ensuring that the computer program of the computerized model and its implementation are correct". And model validation is defined

as the "substantiation that a model within its domain of applicability possesses a satisfactory range of accuracy consistent with the intended application of the model". In this study, the "code verification" is performed by comparing the computational solution with a manufactured analytical solution

in Section 3.2. And the "solution verification" is shown by the quantification of the discretization errors (DEs) in Section 3.3. The fundamental strategy of validation is to assess how accurately the computational results comparing with the experimental data, with quantified error and uncertainty

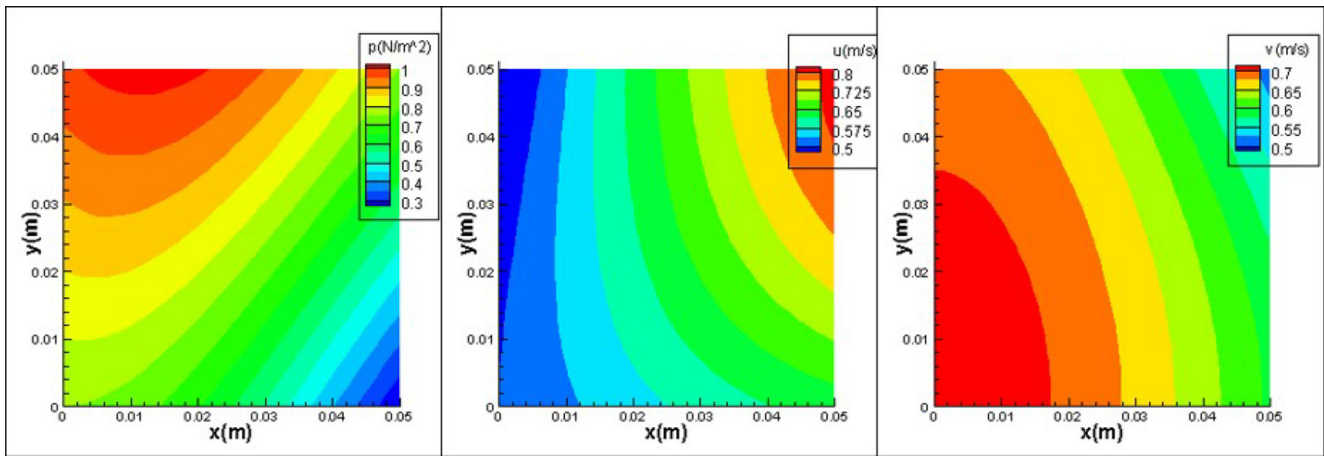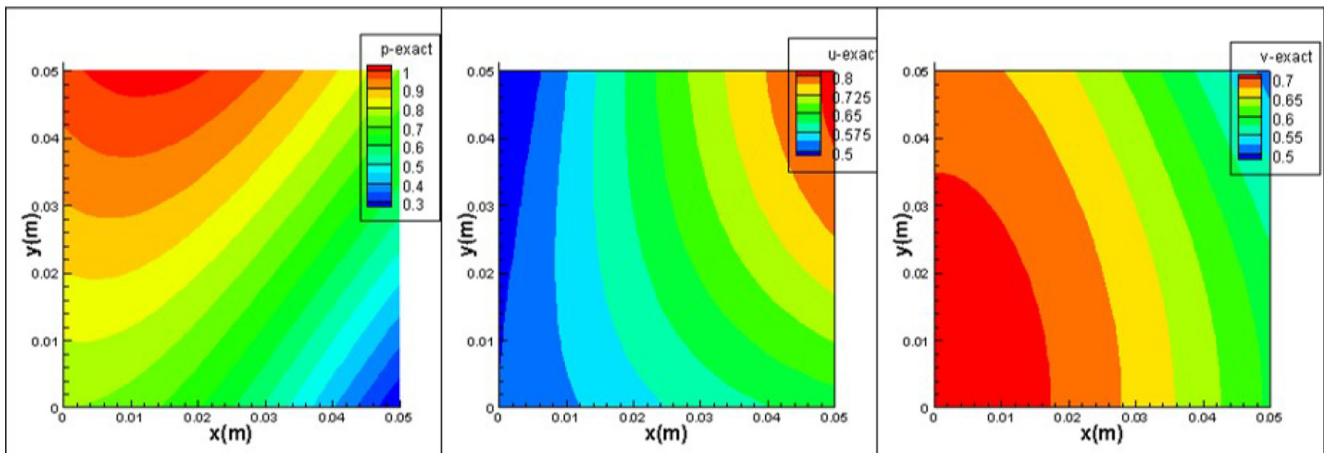**Figure 4** Iteration comparison of the different numerical schemes
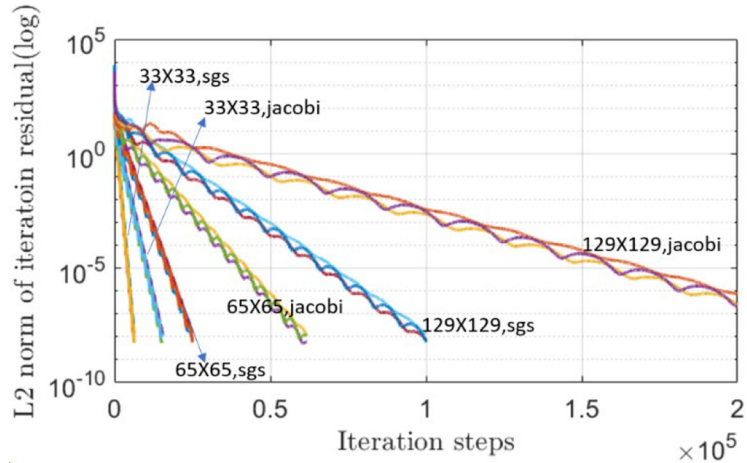
Figure 5 Comparison of (a) manufactured exact solution results with (b) numerical solution

(a)

(b)

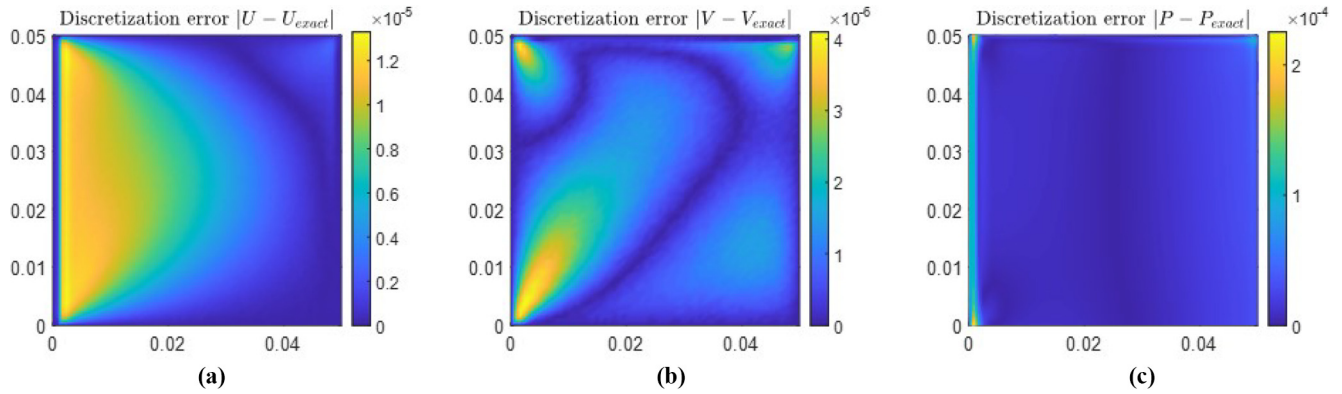**Figure 6** DE for each of three variables (a) u, (b) v and (c) p

(a)   (b)   (c)

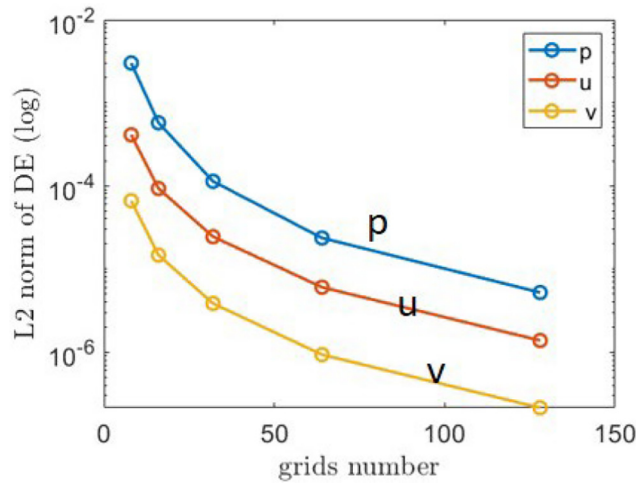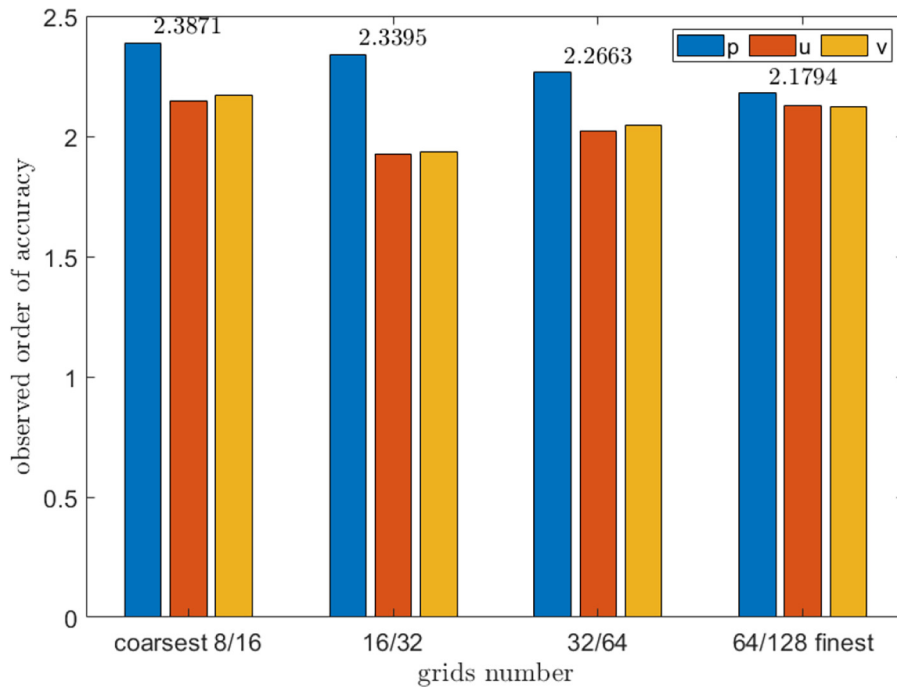**Figure 7** L2 Norms of DE for each of three variables

Figure 8 OOA for each of three variables *p*, u, v from left to right

estimates for both. Here the "Ansys Fluent" solution (Section 3.4) and a benchmark solution (Section 3.5) are used as the "real" phenomenal data because both solutions are validated extensively by researchers. In Section 3.6, the Reynolds number effect is analyzed using this verified and validated numerical model.

3.1 Residual history for p, u and v

To verify the methods implemented, one would like to compare the solution to an exact solution for the flow. This is often not possible as an analytic and exact solution could be nonexistent or unknown. Therefore, this study will use a method of manufactured solution (MMS), in which we prescribe an analytic solution and add source terms to the original equations ensuring they are satisfied based on the prescribed functions of p_{mms}, u_{mms}, v_{mms}. The resulting system is given in equations (24)–(26). Where f_{mass}, $f_{x\text{-}momentum}$, $f_{y\text{-}momentum}$ are determined correspondingly by inputting $p_{mms}(x,y)$, $u_{mms}(x,y)$, $v_{mms}(x,y)$ into the governing equations:

$$\rho \frac{\partial u}{\partial x} + \rho \frac{\partial v}{\partial y} = f_{mass}(x,y) \qquad (24)$$

$$\frac{\partial u}{\partial t} + \rho u \frac{\partial u}{\partial x} + \rho v \frac{\partial u}{\partial y} + \frac{\partial p}{\partial x} - \mu \left(\frac{\partial^2 u}{\partial x^2} + \frac{\partial^2 u}{\partial y^2} \right) = f_{x\text{-}momentum}(x,y) \qquad (25)$$

$$\frac{\partial v}{\partial t} + \rho u \frac{\partial v}{\partial x} + \rho v \frac{\partial v}{\partial y} + \frac{\partial p}{\partial y} - \mu \left(\frac{\partial^2 v}{\partial x^2} + \frac{\partial^2 v}{\partial y^2} \right) = f_{y\text{-}momentum}(x,y) \qquad (26)$$

The discretization methods of point SGS and point Jacobi discussed above are implemented to obtain numerical solutions. The results are compared to the exact functions specified in the manufactured solution, with $Re = 10$. To evaluate the accuracy and behavior at a variety of mesh levels, the grid family with a refinement factor of 2 is created including grids with 9, 17, 33, 65 and 129 nodes in a single direction. Above that, the higher grid-level would take more than 200,000 iteration steps to be converged and is time-consuming.

The converging speed of different numerical algorithms of point Jacobi and SGS can be compared in Figure 4. Among different mesh sizes, it could be noticed that the finer mesh, the longer time it takes to converge. Moreover, the PJ is slower than

Figure 9 Comparison of (a) Fluent results; with (b) the current solution for p, u, v fields from left to right

(a)

(b)
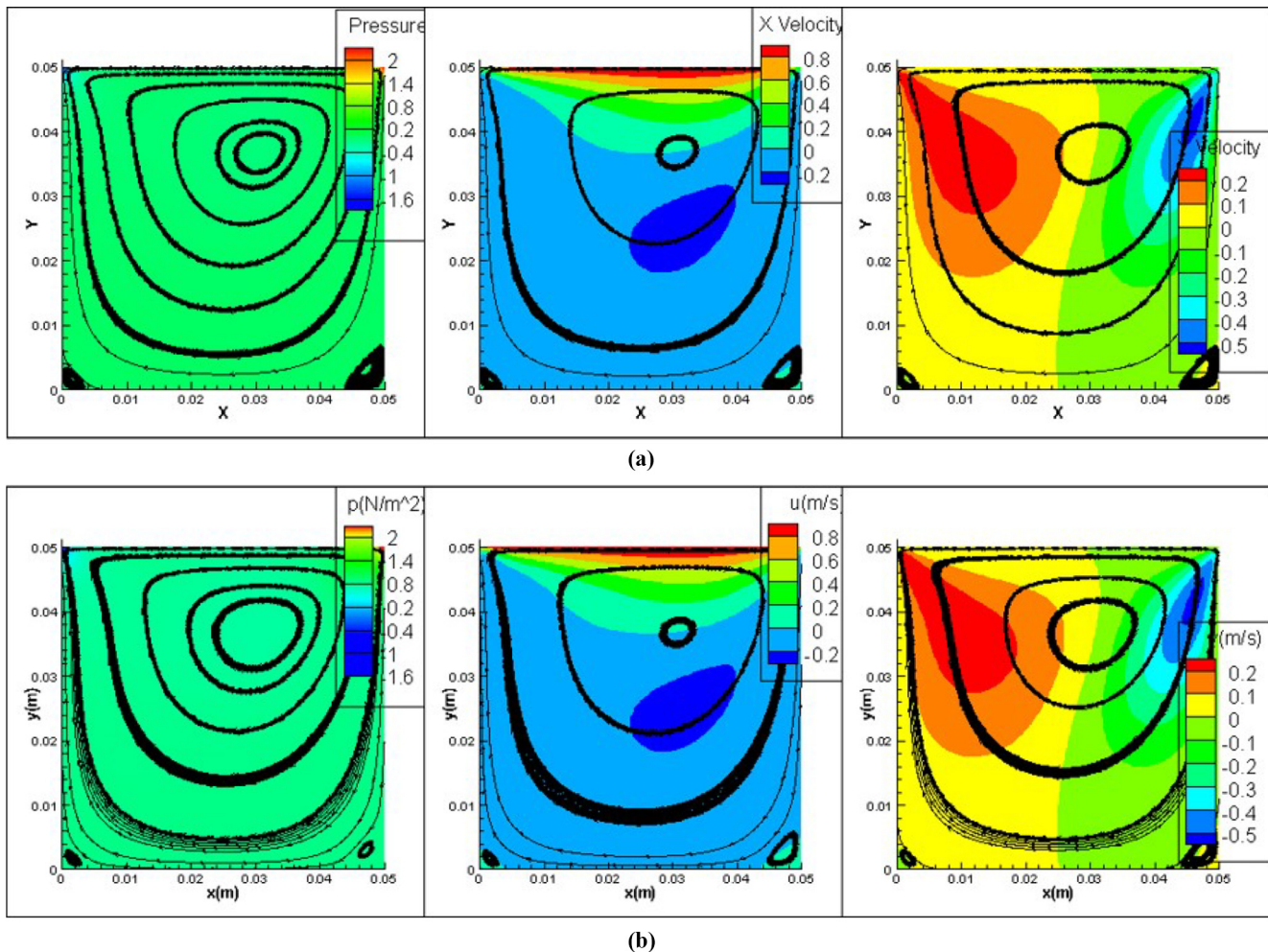
SGS with the same grid level, for instance, SGS is almost three times faster in the 129×129 case. This is because the PJ scheme does not use the updated results in the current iteration. Conversely, SGS can perform "two sub-iterations" in a single iteration step with an updated value obtained in the current iteration. Therefore, the Gauss-Seidel scheme has a higher degree of implicitness than the Jacobi method, and yields faster convergence. As indicated by Mazumder (2015), the added implicitness would manifest itself only if the sweeping pattern is strictly adhered to, whatever that might be. Otherwise, the convergence behavior may revert to that of the Jacobi method.

3.2 Comparison with manufactured solutions
The contour plots of the Numerical Solution of MMS [Figure 5(a)] and MMS exact solution [Figure 5(b)] are compared. At a mesh level of 65×65, it is hard to notice substantial differences between the numerical solution and the manufactured exact solution. It proves that the solution using the point-Jacobi or SGS algorithm can be verified as an accurate approximation to the solution of the discrete equations.

3.3 Discretization error and observed order of accuracy
The discretization error (DE) of the 65×65 grid case is shown in Figure 6. As expected, the DE values are low enough as less than 10^{-4}. The values prescribed at the domain boundaries have no error, but error starts occurring near the boundary as the derivatives at this location are approximated by the solution.

To study the behavior of the DE with mesh size, the L2 norms of the DE for each of the three variables are shown in Figure 7. The mesh sizes are chosen as 9×9, 17×17, 33×33, 65×65, 129×129, and the iteration method is SGS. As the

mesh is refined, the DE is expected to diminish at a rate consistent with the discretization scheme. As the scheme used here is second-order in space, it would be expected that the slope to be consistent with a second-order slope.

The second-order accuracy can also be shown by plotting the observed order of accuracy (OOA) which is a natural logarithm ratio of DEs divided by the natural logarithm of corresponding mesh spacing, for instance, 8 and 16 or 64 and 128. As shown in Figure 8, which shows that the accuracies of the three variables p, u, v are around 2. The discrepancy or uncertainty in the methods could be the influence of time derivative preconditioning or due to the insufficiency of the artificial viscosity term to overcome the odd-even decoupling. With finer

Figure 11 Comparison of current solution with results from the literature for centerline velocity
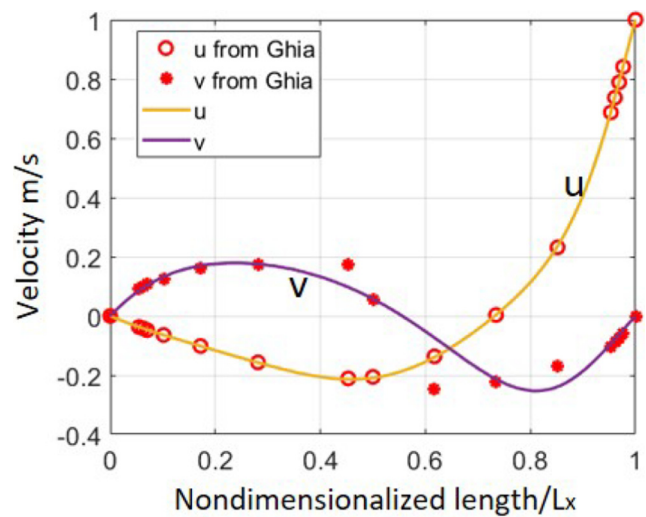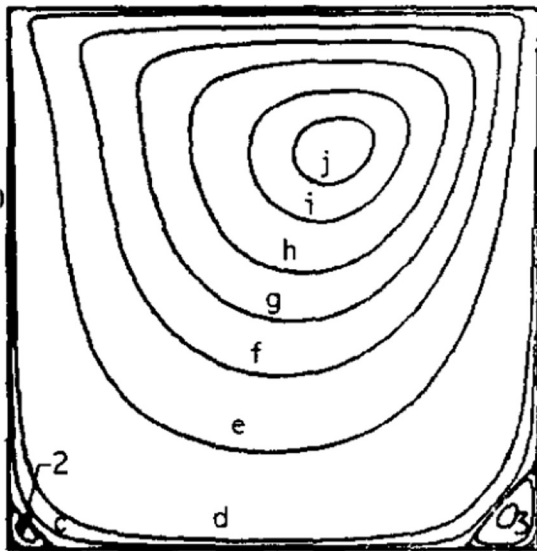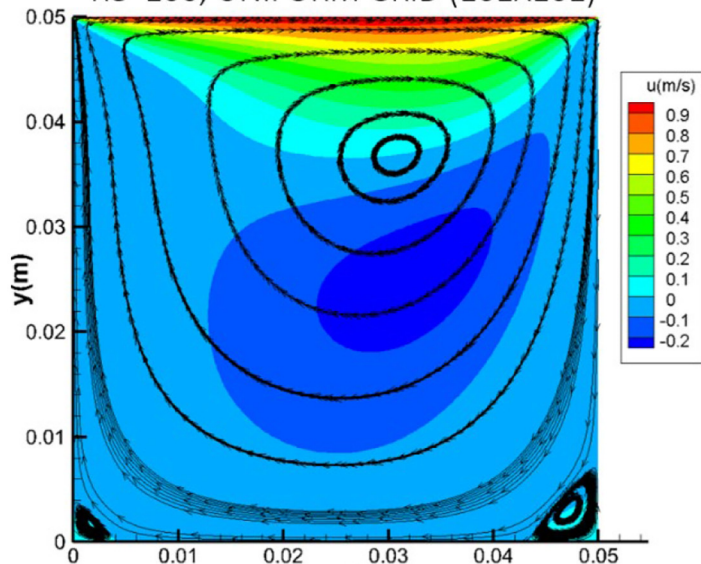

Figure 10 Comparison of (a) literature results; with the (b) current solution


(a)

(b)

mesh, the OOA becomes closer to the expected order of 2 (see the rightmost 64/128 finest case).

3.4 Comparison with commercial software solutions

As a replacement for experimental data, the well-established solutions are used to validate current outputs with the same assumptions, grids, boundary conditions, etc. In this section, the physical issue of driven-cavity is solved and validated with the ANSYS Fluent solutions at Reynolds number of 100. All the boundary conditions are specified to be consistent with the implementation described above. The density of the fluid is set to unity and the dynamic viscosity is used to control the

Figure 12 Vortex formation for Reynolds numbers of (a)100, (b) 500, (c) 1,000 with *p*, u, v fields from left to right

(a)

(b)

(c)
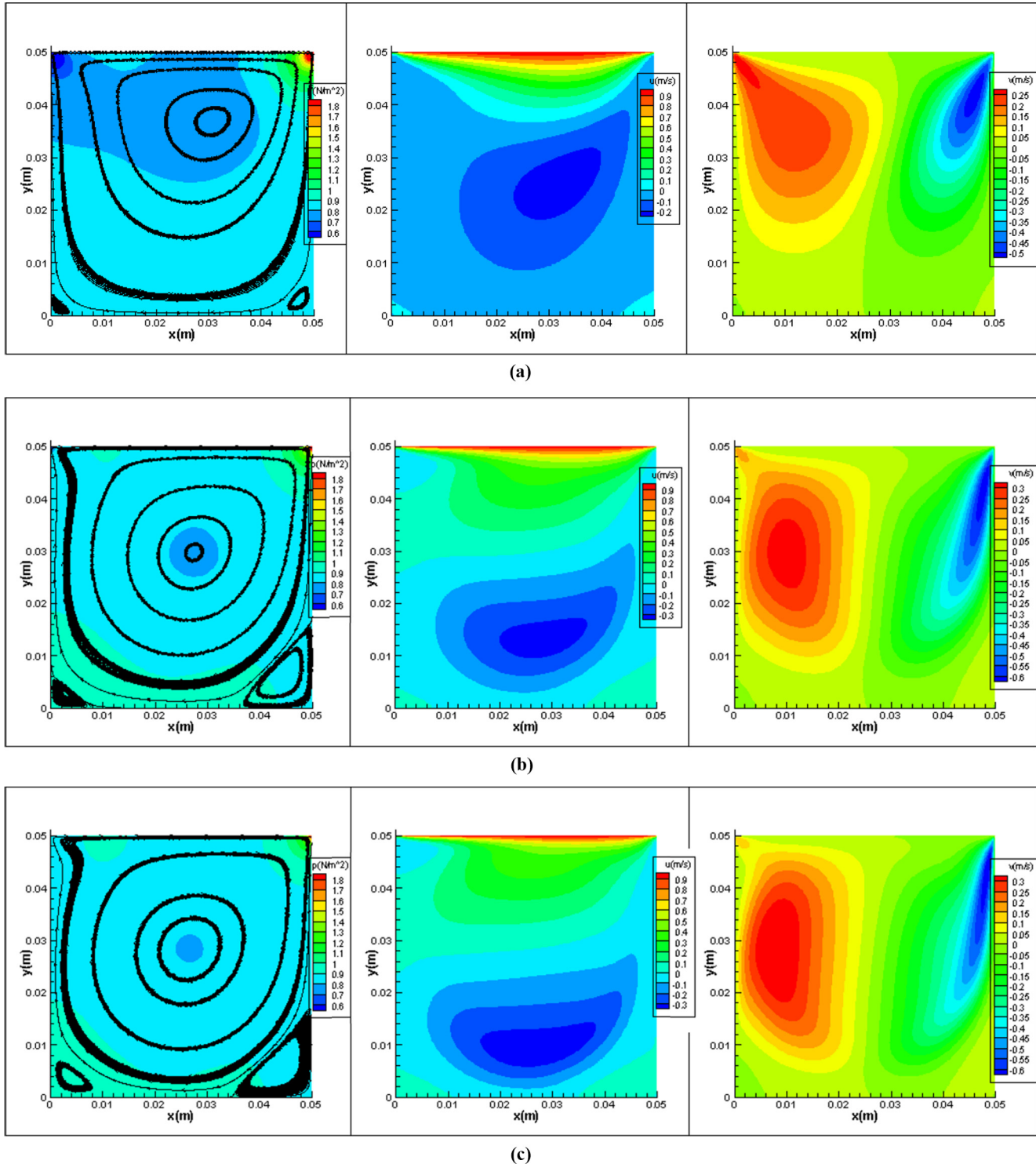
Reynolds number of the flow, which is not equal to the actual fluid property. The case is initialized and run to a convergence tolerance of 1e-8. The results for a Reynolds number of 100 with 81×81 grids are compared in Figure 9. It can be seen that the solutions are nearly identical. Fluent uses a pressure correction method known as the Semi-Implicit Method for Pressure-Linked Equations (SIMPLE), which is widely used and validated for half a century.

3.5 Comparison with the literature

To better understand the accuracy of the current algorithm, the streamlines and velocity distribution along the central line are compared to the benchmark solution gained by Ghia (1982). The results are shown in Figures 10 and 11, in which u is along the vertical centreline while v is along the horizontal centreline. It could be noticed that the similarity of the streamline and velocity components solutions. This provides further validation that the methods used properly produce results that are accurate enough.

3.6 Reynolds number effects

Despite the rising interest in the transition Reynolds number, it cannot be denied the low to medium Re cavity problem still be analyzed with various additional problem modifications. The cases of three different Reynolds numbers $Re = 100$, 500 and 1,000 are chosen to analyze the effect of Re with the same mesh size of 121×121. These effects can be seen in Figures 12(a)–12(c). The resulting flow field shows three different swirling flow structures, which include one primary vortex core in the center and two secondary vortices of USE (upstream secondary eddy) and DSE (downstream secondary eddy) defined by Chiang (1998). The size differences between pairs of smaller vortices at the bottom corner are noticeable comparing three pressure field plots (left). As Re increases, the low-pressure zone becomes smaller while the size of the two smaller circulation vortices in each corner increases. Similar to gears, viscous forces at the lid drive the large core structure which then drives the smaller corner eddies. As the Reynolds number increases, the lid's velocity imposes a relatively

less viscous effect on the adjacent fluid compared with the inertial effect. As time goes by, the strength from inertial forces from the incoming flow made the small vortex, especially DSE at the preferred right corner, increase in size as there is less viscous shear resistance. From u-velocity plots (middle), the negative u-velocity zone becomes lower and wider. While for v-velocity plots (right), the negative v-velocity zone becomes thinner and longer. These phenomena are consistent with the experimental results and can be explained by a higher mass transfer rate of the fluid inside the cavity as Re increases (Sahak *et al.*, 2020). From all these findings, the flow topology is proved to be highly dependent upon the Reynolds number.

4. Parametric effects on numerical behavior

4.1 Mesh size influence on convergence

Mesh size from coarsest 11×11 to finest 161×161 are compared with $Re = 100$, $CFL = 0.5$, $\times = 0.1$, $C^{(4)} = 0.01$ and SGS method. From Figure 13, it can be seen that the mesh size has a significant influence on convergence. For the coarsest 11×11 grid level, the spatial resolution has deviated too much that leading to divergence in a short time. Excluding that, a finer mesh typically requires more iterations and time to converge. Two facts account for this as follows: on the one hand, as mesh size decreases, smaller time steps need to be used due to the stability criteria; on the other hand, as the artificial viscosity term is of magnitude Δx^3, the residual which comes from artificial viscosity will decrease, which needs more iterations to shrink the DE between discretized equations with artificial viscosity and physical equations. Results (in terms of iteration steps trend) agree well with the CFD simulation of an engine nacelle by Olejnik *et al.* (2021).

4.2 Mesh size sensitivity

As stated by Erturk (2005), the accuracy of a finite difference solution is set by the mesh size, and by the spatial order of the FD equations and the boundary approximations. Therefore, mesh fineness is not only a very influential parameter to the

Figure 13 Residual history comparison for different grid sizes 11, 21, 41, 81, 121 and 161
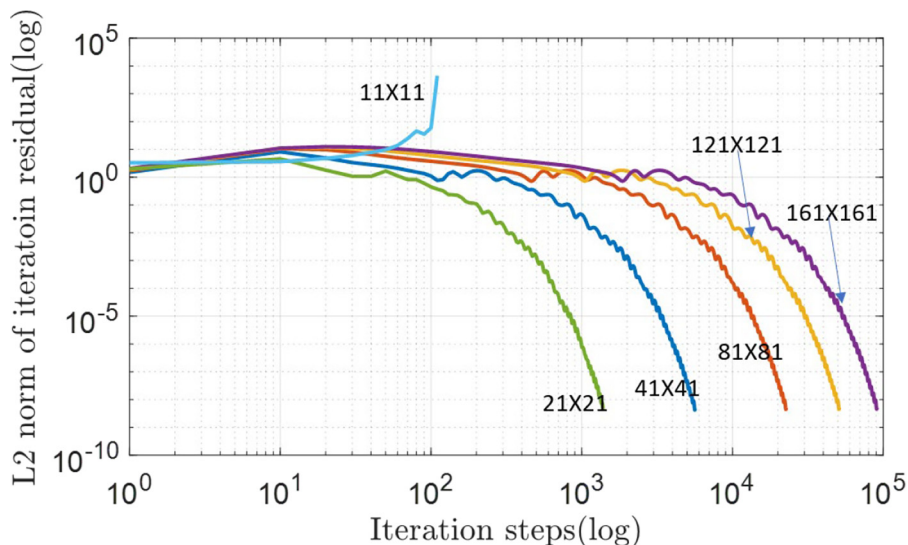
computation speed but also the solution accuracy. As the number of nodes grows, the steps are made smaller and more computations per time step are required. This motivates the need to determine an efficient but also sufficiently small size based upon results. The influence of mesh size on the flow field solution accuracy is shown in Figure 14. For the 21×21 and 41×41 grid cases, the edges of the blue color area (v component of reversed y-direction) are irregular in these coarser meshes as they are not able to be resolved accurately. From cases of 81×81 and 161×161 grid levels, it is apparent that the mesh size does not have a significant influence on the solution. It is confirmed that the 81×81 medium size of the current domain is large enough for an accurate prediction, which is consistent with the computational study of an airfoil by Duddempudi *et al.* (2007). For finer mesh cases, the v component contour lines are arranged much smoother as approaching a more accurate solution. As the number of grids

used increases, the mesh size Δh gets smaller. Defined as $Re_c = u\Delta h/v$, this cell Reynolds number Re_c or so-called Peclet number decreases as well. Thus, the small corner vortices can be resolved better enabling an accurate solution, and the numerical stability characteristics are also improved.

4.3 Influence of prescribed κ value

As stated in Section 2.2, with the time-derivative preconditioning term the resultant scheme becomes a symmetric hyperbolic system for the inviscid terms, which is called a well-posed system. Numerical methods can be used with marching this hyperbolic system in time. The parameter β added can be chosen to accelerate the convergence to the steady-state.

To study the effects of this β term, cases with five different values of κ which multiplying the lid velocity in the determination of β when the x-component of velocity is small [Equation (5)], are investigated. The parameters are chosen as

Figure 14 Solutions for grid sizes of 21, 41, 81 and 161
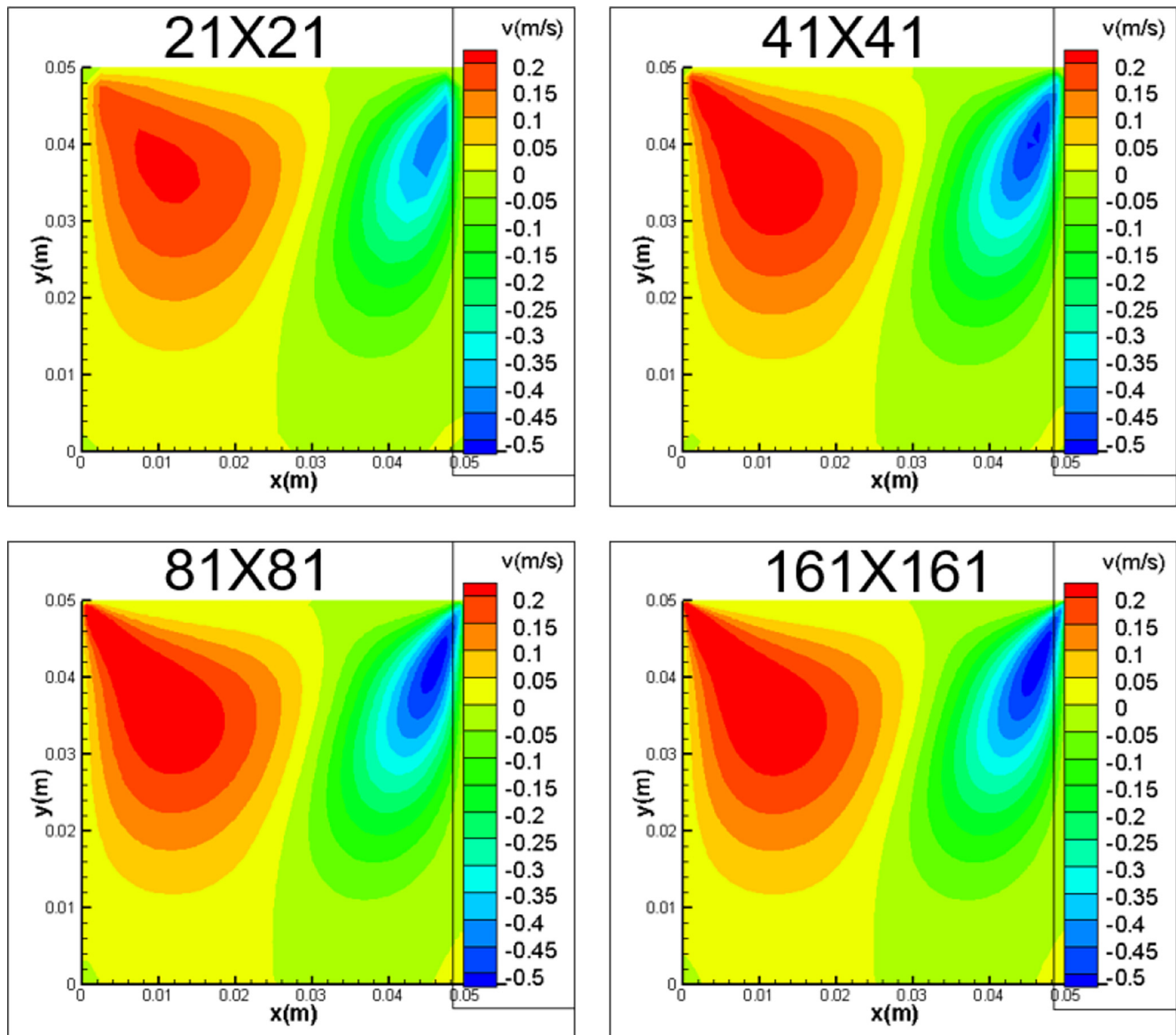
grids 65×65, $Re = 100$, $CFL = 0.5$, $\kappa = [0.001, 0.01, 0.1, 0.3, 0.9]$, and $C^{(4)} = 0.01$. The resulting convergence histories can be seen in Figure 15. For larger values of κ, the maximum of $u^2 + v^2$ for the inside nodes are always smaller than κU^2 throughout the iteration. Thus, the value of κ ranging from 0.01 to 0.9 will not generate significantly different convergence times. When κ is as small as 0.001, β would be determined by $u^2 + v^2$ leading to a relatively large pseudo-time derivative of $\frac{1}{\beta^2}\frac{\partial p}{\partial t}$ which significantly affect the numerical behavior of the solution. Because β is updated locally at each node, instead of a constant, that the algorithm takes a much longer time to converge. Therefore, though a smaller κ inducing a larger $\frac{1}{\beta}$ would enhance the computation stability, it shall be selected without significantly slowing the computation or destroying the time accuracy of the governing equations.

4.4 Effects of artificial viscosity

The exact value of the coefficient $C^{(4)}$ multiplying in the artificial viscosity term has the potential to influence flow solutions because it can add too much viscosity to the slower waves (Turkel and Vatsa, 1994). The numerical parameters studied are chosen as $CFL = 0.5$, $\kappa = 0.1$, $C^{(4)} = [\frac{1}{16}, \frac{1}{32}, \frac{1}{64}, \frac{1}{100}$ and $\frac{1}{128}]$. The DE versus $\times$ from 0 to 0.05 m at the centerlines of $y = 0.025$ m is calculated for MMS solutions. As shown in Figure 16(a), with increasing of $C^{(4)}$ from 1/128 to 1/16, the peaks of absolute DE of the u-component increase proportionally from 1e-5 to 8e-5 by 8 times. A similar trend can be observed from Figure 16(b) for DE of the v-component and Figure 16(c) for DE of the pressure with different significance. Undoubtedly, a lower $C^{(4)}$ means the calculation is less affected by artificial viscosity, thus a more accurate solution. However, the odd-even decoupling issue could be seen for low enough values of this coefficient, that numerical values could oscillate between adjacent nodes. In sum, this coefficient $C^{(4)}$ shall be selected wisely as a compromise of mitigating DE and odd-even decoupling effects using a preliminary test.

5. Conclusion

The cavity flows arise extensively in aerospace industrial applications, such as structural integrity analysis, noise control and CFD solver verification. This paper presents an extensive review of the literature about the CFD development in LDC flow, discusses methods and procedures for assessing V&V and explained fundamental issues, such as code verification, solution V&V. A detailed parametric study introduces the best way to choose a rapid and effective numerical setting when applying LDC flow as a validation tool for the new solver development. The detailed design suggestions can be summarized as follows:

- The SGS Method can be more than three times faster (or fewer iteration steps) than the Jacobi method at the same parameter settings, implying that the more implicit the iterative scheme, the faster the convergence. From the verification with MMS, the OOA is gradually converged to two which is the formal order of accuracy for both iteration methods. Both schemes have the advantage that they are time-saving to implement and are applicable to any mesh topology. And the computational cost per iteration of both methods is also very low, making them attractive choices.

- For different Reynolds numbers, the flow structures are different due to viscous effects with different μ. Until the Reynolds number reaches 100, the corner eddies near the lid plane are small even hardly visible. For Reynolds numbers approaching 500 to 1,000, the primary core moves to the center, and the DSE/USE starts to grow and detach from the side walls. At higher Reynolds numbers, steady numerical solutions can only be obtained using finer grid meshes, otherwise, results would be periodic.

- Finer meshes require more time steps to converge while coarse mesh can be more easily driven unstable. Our computations indicate that the DE norm is decreased with the mesh size decreasing. Therefore, finer grid mesh is necessary to obtain a steady solution and also resolve the vortices that appear at the corners of the cavity, especially at high Reynolds number cases.

- Time-derivative preconditioning is necessary to the stability of the scheme and κ must be sufficiently large to allow stability. The effects of artificial viscosity can be observed by changing $C^{(4)}$, and artificial viscosity would proportionally affect the value of DE.

Figure 15 Residual history comparison for different time-derivative preconditioning factors
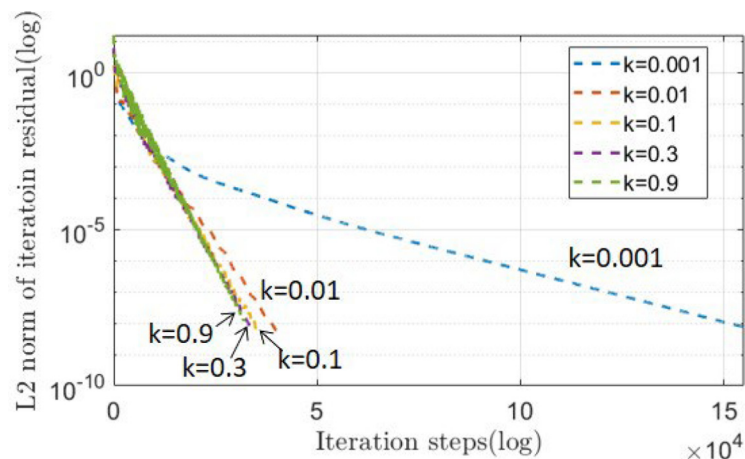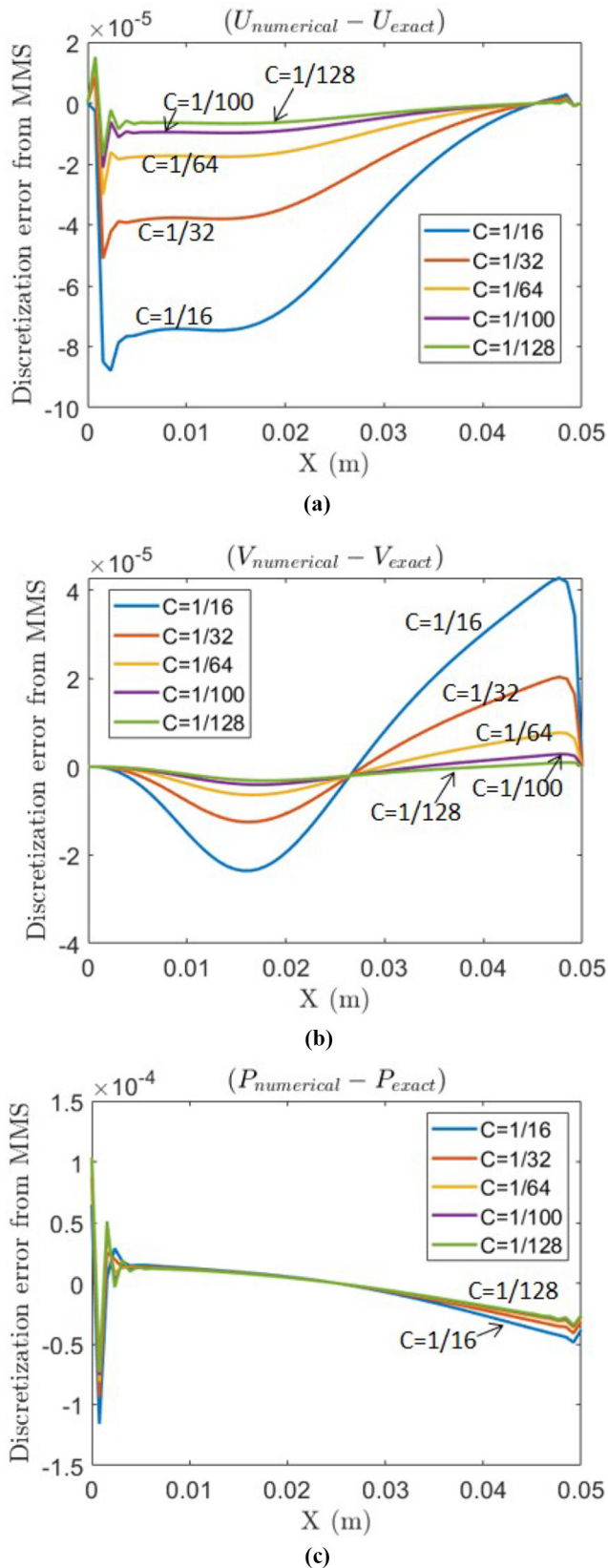
Figure 16 DE of (a) u-component; (b) v-component; (c) pressure at the left wall for different constants used in the artificial viscosity formulation

(a)

(b)

(c)

References

AbdelMigid, T.A., Saqr, K.M., Kotb, M.A. and Aboelfarag, A.A. (2017), "Revisiting the lid-driven cavity flow problem: review and new steady state benchmarking results using GPU accelerated code", *Alexandria Engineering Journal*, Vol. 56 No. 1, pp. 123-135.

Abderrahmane, B., Rezoug, T. and Dala, L. (2019), "Passive control of cavity acoustics via the use of surface waviness at subsonic flow", *Aircraft Engineering and Aerospace Technology*, Vol. 91 No. 2.

Albensoeder, S. and Kuhlmann, H.C. (2005), "Accurate three-dimensional lid-driven cavity flow", *Journal of Computational Physics*, Vol. 206 No. 2, pp. 536-558.

Barragy, E. and Carey, G.F. (1997), "Stream function-vorticity driven cavity solution using *p* finite elements", *Computers & Fluids*, Vol. 26 No. 5, pp. 453-468.

Botella, O. and Peyret, R. (1998), "Benchmark spectral results on the lid-driven cavity flow", *Computers & Fluids*, Vol. 27 No. 4, pp. 421-433.

Bouffanais, R., Deville, M.O. and Leriche, E. (2007), "Large-eddy simulation of the flow in a lid-driven cubical cavity", *Physics of Fluids*, Vol. 19 No. 5, p. 055108.

Brindhadevi, K., Shanmuganathan, R., Pugazhendhi, A., Gunasekar, P. and Manigandan, S. (2021), "Biohydrogen production using horizontal and vertical continuous stirred tank reactor-a numerical optimization", *International Journal of Hydrogen Energy*, Vol. 46 No. 20, pp. 11305-11312.

Bruneau, C.H. and Saad, M. (2006), "The 2D lid-driven cavity problem revisited", *Computers & Fluids*, Vol. 35 No. 3, pp. 326-348.

Burggraf, O.R. (1966), "Analytical and numerical studies of the structure of steady separated flows", *Journal of Fluid Mechanics*, Vol. 24 No. 1, pp. 113-151.

Chiang, T.P., Sheu, W.H. and Hwang, R.R. (1998), "Effect of reynolds number on the eddy structure in a lid-driven cavity", *International Journal for Numerical Methods in Fluids*, Vol. 26 No. 5, pp. 557-579.

Duddempudi, D., Yao, Y., Edmondson, D., Yao, J. and Curley, A. (2007), "Computational study of flow over generic fan-wing airfoil", *Aircraft Engineering and Aerospace Technology*, Vol. 79 No. 3.

Erturk, E. (2009), "Discussions on driven cavity flow", *International Journal for Numerical Methods in Fluids*, Vol. 60 No. 3, pp. 275-294.

Erturk, E., Corke, T.C. and Gökçöl, C. (2005), "Numerical solutions of 2-D steady incompressible driven cavity flow at high reynolds numbers", *International Journal for Numerical Methods in Fluids*, Vol. 48 No. 7, pp. 747-774.

Esfahanian, V. and Akbarzadeh, P. (2011), "Numerical investigation on a new local preconditioning method for solving the incompressible inviscid, non-cavitating and cavitating flows", *Journal of the Franklin Institute*, Vol. 348 No. 7, pp. 1208-1230.

Gaikwad, P.U., Gnanamani, S. and Subramani, N. (2021), "Experimental and numerical simulation of the piston engine fueled with alternative fuel blends: CFD approach", *Aircraft Engineering and Aerospace Technology*.

Ge, M., Cheng, X., Huang, W., Hu, R. and Cheng, Y. (2020), "Damage mode and load distribution of countersunk bolted composite joints", *Journal of Composite Materials*, Vol. 55 No. 13, p. 0021998320976782.

Ghadge, R.R. and Prakash, S, (2021), "Weight minimization of fiber laminated composite beam for aircraft wing construction using exhaustive enumeration algorithm and numerical modeling", *Aircraft Engineering and Aerospace Technology*.

Ghia, U.K.N.G., Ghia, K.N. and Shin, C.T. (1982), "High-Re solutions for incompressible flow using the Navier-Stokes equations and a multigrid method", *Journal of Computational Physics*, Vol. 48 No. 3, pp. 387-411.

Goetzendorf-Grabowski, T. and Mieloszyk, J. (2017), "Common computational model for coupling panel method with finite element method", *Aircraft Engineering and Aerospace Technology*, Vol. 89 No. 5.

Groth, C., Cella, U., Costa, E. and Biancolini, M.E. (2019), "Fast high fidelity CFD/CSM fluid structure interaction using RBF mesh morphing and modal superposition method", *Aircraft Engineering and Aerospace Technology*, Vol. 91 No. 6.

Hammami, F., Ben-Cheikh, N., Ben-Beya, B. and Souayeh, B. (2018), "Combined effects of the velocity and the aspect ratios on the bifurcation phenomena in a two-sided lid-driven cavity flow", *International Journal of Numerical Methods for Heat & Fluid Flow*, Vol. 28 No. 4.

Koseff, J.R., Street, R.L., Gresho, P.M., Upson, C.D., Humphrey, J.A. and To, W.M. (1983), "Three-dimensional lid-driven cavity flow: experiment and simulation (no. CONF-830803-11)", Stanford Univ., CA (USA). Dept. of Civil Engineering; Lawrence Livermore National Lab., CA (USA); California Univ., Berkeley (USA). Dept. of Mechanical Engineering.

Kuhlmann, H.C. and Romanò, F. (2019), "The lid-driven cavity", *Computational Modelling of Bifurcations and Instabilities in Fluid Dynamics*, pp. 233-309.

Magalhães, J.P., Albuquerque, D.M., Pereira, J.M. and Pereira, J.C. (2013), "Adaptive mesh finite-volume calculation of 2D lid-cavity corner vortices", *Journal of Computational Physics*, Vol. 243, pp. 365-381.

Mazumder, S. (2015), *Numerical Methods for Partial Differential Equations: finite Difference and Finite Volume Methods*, Academic Press, pp. 123-130.

Mukherjee, S., Shahabi, V., Gowtham, R., Rajan, K.S. and Velamati, R.K. (2019), "Effect of knudsen number, lid velocity and velocity ratio on flow features of single and double lid driven cavities", *Journal of Applied Fluid Mechanics*, Vol. 12 No. 5, pp. 1575-1583.

Olejnik, A., Dziubiński, A. and Kiszkowiak, Ł. (2021), "CFD simulation of engine nacelle cooling on pusher configuration aircraft", *Aircraft Engineering and Aerospace Technology*, Vol. 93 No. 9.

Perumal, D.A. and Dass, A.K. (2011), "Multiplicity of steady solutions in two-dimensional lid-driven cavity flows by lattice Boltzmann method", *Computers & Mathematics with Applications*, Vol. 61 No. 12, pp. 3711-3721.

Sahak, A.S.A., Sidik, N.A.C. and Yusof, S.N.A. (2020), "A brief review of particle dispersion of cavity flow", *Journal of Advanced Research in Applied Sciences and Engineering Technology*, Vol. 20 No. 1, pp. 27-41.

Sargent, R.G. (2013), "Verification and validation of simulation models", *Journal of Simulation*, Vol. 7 No. 1, pp. 12-24.

Shankar, P.N. and Deshpande, M.D. (2000), "Fluid mechanics in the driven cavity", *Annual Review of Fluid Mechanics*, Vol. 32 No. 1, pp. 93-136.

Suman, V.K., Tekriwal, M.K., Bhaumik, S. and Sengupta, T.K. (2019), "Grid sensitivity and role of error in computing a lid-driven cavity problem", *Physical Review E*, Vol. 99 No. 1, p. 013305.

Turkel, E. and Vatsa, V.N. (1994), "Effect of artificial viscosity on three-dimensional flow solutions", *AIAA Journal*, Vol. 32 No. 1, pp. 39-45.

Xia, Y., Xie, Y., Li, D. and Wang, W. (2019), "Numerical analysis of hub cavity leakage", *Aircraft Engineering and Aerospace Technology*, Vol. 91 No. 8.

Zhang, X.L., Ge, M.M., Zhang, G.J. and Coutier-Delgosha, O. (2021), "Compressible effects modeling for turbulent cavitating flow in a small venturi channel: an empirical turbulent eddy viscosity correction", *Physics of Fluids*, Vol. 33 No. 3, p. 035148.

Further reading

Peng, Y.F., Shiau, Y.H. and Hwang, R.R. (2003), "Transition in a 2-D lid-driven cavity flow", *Computers & Fluids*, Vol. 32 No. 3, pp. 337-352.

Corresponding author

Olivier Coutier-Delgosha can be contacted at: ocoutier@vt.edu